Improving Exoskeleton Brace Design: Alleviating Misalignment and Parasitic Forces

Suleyman Can Cevik
Dept. of Mechanical Engineering
Ozyegin University
Cekmekoy, Istanbul 34794
Türkiye
Email: suleyman.cevik@ozu.edu.tr

Ahmed Fahmy Soliman
Dept. of Electrical and Electronic Engineering
The University of Manchester
RAICo1, Whitehaven, CA28 6AU
United Kingdom
Email: ahmed.soliman@manchester.ac.uk

Mustafa Derman
Dept. of Mechanical Engineering
Ozyegin University
Cekmekoy, Istanbul 34794
Türkiye
Email: mustafa.derman@ozu.edu.tr

Sinan Coruk
Robotics and Multibody Mech. Res. Gr.
Vrije Universiteit Brussel
1050 Brussel
Belgium
Email: sinan.coruk@vub.be

Ramazan Unal
Dept. of Mechanical Engineering
Ozyegin University
Cekmekoy, Istanbul 34794
Türkiye
Email: ramazan.unal@ozyegin.edu.tr

Barkan Ugurlu
Dept. of Mechanical Engineering
Ozyegin University
Cekmekoy, Istanbul 34794
Türkiye
Email: barkan.ugurlu@ozyegin.edu.tr

Ozkan Bebek*
Dept. of Mechanical Engineering
Ozyegin University
Cekmekoy, Istanbul 34794
Türkiye
Email: ozkan.bebek@ozyegin.edu.tr

ABSTRACT

This article presents a design methodology for exoskeleton-user connection attachments, i.e., braces, that aims to reduce parasitic forces and potentially improve user comfort. The proposed brace structure incorporates additional passive joints, identified through a hyperstaticity analysis to minimize undesired tangential forces, e.g., rubbing against the user skin. To assess the proposed structure, we primarily conducted simulation experiments using a human-exoskeleton coupled model in an MSC-ADAMS environment. Subsequently, a series of real-life experiments was conducted using a self-balancing bipedal exoskeleton with two distinct dummy manikins. The results demonstrated the feasibility of the proposed brace structure in reducing the parasitic forces and slippage compared to conventional fixation approach.

1 INTRODUCTION

In the last two decades, we have witnessed dramatic advancements in wearable technologies, particularly owing to their applications in power augmentation and healthcare [1, 2, 3, 4]. Although some studies have questioned the feasibility of these devices [5, 6], systematic reviews suggest promising future opportunities in these fields provided that persistent issues are addressed. [7, 8].

One of the major persistent challenges is the

*Corresponding author: ozkan.bebek@ozyegin.edu.tr

unavoidable joint misalignment between robot and human joints, as they belong to distinct kinematic chains [9]. Unlike robot joints, human joint axes may shift during the course of movement [10], which further complicates alignment. This issue leads to tangential parasitic forces, which may make the use of exoskeleton an uncomfortable experience for humans and reduce safety to the point of excess pain or joint dislocation [11, 12].

In reducing the problems that arise due to joint misalignment, researchers developed exoskeletons with adjustable links [13, 14]. While useful in its own right, this approach may not fully minimize the misalignment since human joint structures are complex and their axis of rotation undergoes displacement when performing complex tasks [15]. Therefore, failure in accurate alignment to human body anatomical structure would again lead to parasitic force. Although the usage of soft materials with adjustable exoskeleton links would effectively dampen the parasitic force, the long-term usability is still questionable [9, 16].

In response to this matter, researchers developed self-aligning mechanisms where additional joints are placed on the exoskeleton links to match the robot to human joint axes [10, 17, 18, 19, 20, 21, 22]. This design approach provides an on-the-fly adaptation to the human joints' rotation axis variation. It also significantly reduces the donning (i.e., device on) time, which is crucial for several applications [23]. On the contrary, it could lead to technical issues, e.g., complicated mechanisms, increased weight and size, and modeling uncertainties due to kinematic loops [24]. Therefore, using complex mechanisms in lower-body exoskeletons could increase power and energy demands, which contradicts its primary design considerations [25].

As an alternative, a series of passive degrees of freedom (DOF) can be introduced between the exoskeleton links and the braces [26, 27]. This allows the brace to adapt its posture passively in a way so as to minimize misalignment between the exoskeleton and human joints, provided that hyperstaticity analysis is conducted. Compared to self-aligning mechanisms [10, 21], it is relatively less complex and does not involve additional kinematic loops. Consequently, it offers an efficient solution and it was implemented to upper limb exoskeleton devices [26, 27].

Building on the foundational research presented in [27], this paper presents a novel exoskeleton brace that can enhance the human-robot coupling functionality for self-balancing lower-body exoskeletons. With the advent of such self-balancing exoskeletons [25, 28, 29], the development of effective coupling braces has become a critical necessity. In response to this need, this paper investigates this issue and offers three contributions: i) through a hyperstaticity analysis, the required configuration of passive degrees of freedom for the novel brace was identified and it was manufactured for experimental verification in the context of a self-balancing exoskeleton [25], ii) utilizing a segmented, watch strap-like bedding inspired by the design in [30], the proposed brace integrates multiple force sensing elements to enable in-situ measurements without impeding exoskeleton mobility, iii) parasitic forces and contact stability were quantitatively assessed in experiments via in-situ measurements.

The rest of the paper is structured as follows: Section II discusses the methods used to develop the proposed brace. Section III presents the experimental setup. Section IV discusses the experimental results. Finally, the paper is concluded in the last section.

2 METHODS

2.1 Identifying the Passive DOFs for Fixation

To systematically identify the passive joints' configuration of the proposed the brace, we consider human with n bodies connected to exoskeleton links through n fixations; see Fig. 1. The human and exoskeleton bodies are given as $\mathcal{H}_i$ and $\mathcal{E}_i$, respectively, where $i \in \{1, 2, ..., n\}$. Each human body is attached to the exoskeleton via a brace. Each brace is connected to the exoskeleton link through mechanism $\mathbf{L}_i(l_i)$ with connectivity $0 \leq l_i \leq 5$, where the connectivity means the minimum number of joints required to achieve the targeted mechanism structure [26]. For $l_i = 0$, the connection between the exoskeleton and brace is completely rigid, and $l_i = 6$ corresponds to an unconnected brace. To determine each l_i, we used a method similar to the one explained in [27].

Considering a human user in a static posture, with the trunk rigidly attached to the exoskeleton base, a mechanism subsystem $\mathbf{M}_i$, which connects the human to the exoskeleton body $\mathcal{E}_i$ is illustrated in Fig. 1. The connectivity m_i of the mechanism chain $\mathbf{M}_i$ can be determined recursively based on the connectivity e_i of the mechanism chain $\mathbf{E}_i(e_i)$, the connectivity l_i of $\mathbf{L}_i(l_i)$, and the preceding value m_{i-1}. The connectivity equation of the closed-loop chain shown in Fig. 1 can be written using vector subspaces as follows [31]:

$$\dim(V(\mathbf{M}_i)) = \dim(V(\mathbf{L}_i) \cap (V(\mathbf{E}_i) + V(\mathbf{M}_{i-1}))) \quad (1)$$

where $V(\bullet)$ denotes the vector space, and the connectivity m_i is given as $m_i = \dim(V(\mathbf{M}_i))$. Furthermore, by investigating the schematic chain depicted in Fig. 1, the following physical conditions are

imposed to ensure force transmission with reduced parasitic forces.

1) The open-chain mobility $\mathbf{M}_{i-1} - \mathbf{E}_i - \mathbf{L}_i$ should be 6. In other words, it should be capable of moving in any position and orientation in the Cartesian space. This condition can be expressed as below:

$$\dim(V(\mathbf{L}_i) + V(\mathbf{E}_i) + V(\mathbf{M}_{i-1})) = 6. \tag{2}$$

2) When the body $\mathcal{E}_i$ stopped, no possible motion should exist for $\mathcal{E}_{i-1}$. As a result, motion redundancy is avoided, and uncontrolled motion is prevented. This condition is equivalent to the following:

$$\dim(V(\mathbf{M}_{i-1}) \cap V(\mathbf{E}_i)) = 0. \tag{3}$$

3) No motion should occur between the human body and the exoskeleton body $\mathcal{E}_n$. Consequently, the mechanism subsystem $\mathbf{M}_n$ is fully constrained. This condition can be represented as follows:

$$\dim(V(\mathbf{M}_n)) = 0. \tag{4}$$

By applying $\dim(\mathbf{x}) + \dim(\mathbf{y}) = \dim(\mathbf{x} + \mathbf{y}) + \dim(\mathbf{x} \cap \mathbf{y})$, for any two arbitrary vector subspaces $\mathbf{x}$ and $\mathbf{y}$, and using the equations (1)-(3), the following equation can be derived:

$$m_i = l_i + e_i + m_{i-1} - 6. \tag{5}$$

In (5), m_0 should be equal to 0 since the human trunk and exoskeleton base are rigidly attached. Using the recursive structure of (5), a simpler form can be yielded:

$$m_i = \sum_{j=1}^{i} (l_j + e_j) - 6i. \tag{6}$$

By applying the mathematical rule stating, $\dim(\mathbf{x} + \mathbf{y} + \mathbf{z}) \leq \dim(\mathbf{x}) + \dim(\mathbf{y}) + \dim(\mathbf{z})$ for any arbitrary vector subspaces $\mathbf{x}$, $\mathbf{y}$, and $\mathbf{z}$ to the eq. (2), the inequality $l_i + e_i + m_{i-1} \geq 6$ can be derived. Using Eq. (6), the inequality can be expressed as follows:

$$\sum_{j=1}^{i} (l_j + e_j) \geq 6i. \tag{7}$$

The eq. (7) is used to obtain the minimum number of DOF required to be freed without over-constraints. Since, for any arbitrary subspace vectors $\mathbf{x}$, $\mathbf{y}$ of space $\mathbf{A}$, if $\mathbf{x} \cap \mathbf{y} = \{0\}$, then $\dim(\mathbf{x}) + \dim(\mathbf{y}) \leq \dim(\mathbf{A})$, therefore, equations (3) and (6) can lead to the following:

$$\sum_{j=1}^{i-1} (l_j + e_j) + e_i \leq 6i. \tag{8}$$

Equation (8) is employed to identify the maximum number of DOF that can remain free in the passive mechanism without inducing internal motions. Using the recursive formula from (6), and the condition from (4), the following equality can be derived:

$$\sum_{j=1}^{n} (l_j + e_j) = 6n. \tag{9}$$

The equality in (9) is used to calculate the total DOF that must be freed by the passive mechanism.

The valid connectivity configuration may differ depending on the gait; when the leg is in swing phase, the torso is assumed to be fixed, whereas when the leg is in stance phase, the foot is assumed to be fixed.

2.1.1 *Fixed Torso*

Fig. 2(a) shows the kinematic chains connecting human segments to a lower-body-exoskeleton base and its individual links concerning a single leg for the case of fixed torso. The symbols $(\mathcal{E}_0, \mathcal{E}_1, \mathcal{E}_2, \mathcal{E}_3)$ corresponds to exoskeleton base, thigh, shank, and foot, respectively. The symbols $(\mathbf{E}_1, \mathbf{E}_2, \mathbf{E}_3)$ corresponds to exoskeleton's 2-DOF hip joint $(e_1 = 2)$, 1-DOF knee joint $(e_2 = 1)$, and 1-DOF ankle joint $(e_3 = 1)$, respectively. The minimum and maximum values for the connectivity $4 \leq l_1 \leq 5$ is obtained using the eqs. (7) and (8). The upper limit for the number of joints is 5; otherwise, the connection does not exist. Similarly, the maximum and minimum values for the connectivity l_2 are obtained via (7) and (8) such that, $l_1 + l_2 \geq 9$ and $l_1 + l_2 \leq 14$. Using Eq. (9), and number of connection points $n = 3$ the total number of passive joints is $(l_1 + l_2 + l_3 = 14)$. As next step, the connectivity l_3 is obtained such that the total number of joints is 14. Consequently, the valid connectivity combinations for (l_1, l_2, l_3) are $(4, 5, 5)$, $(5, 4, 5)$, and $(5, 5, 4)$.

2.1.2 *Fixed Foot*

Fig. 2(b) illustrates the kinematic chains connecting human segments to a lower-body exoskeleton base and its individual links for a single leg with a fixed foot. In this analysis, each exoskeleton leg is considered separately, and the individual links are rearranged so that the initial body $\mathcal{E}_0$ represents the exoskeleton foot. The exoskeleton shank and thigh

are denoted as $\mathcal{E}_1$ and $\mathcal{E}_2$, respectively. Braces with passive joints are used exclusively to attach the human shank and thigh to the exoskeleton links. For this configuration, $n = 2$, and the connectivities e_1 and e_2 correspond to the ankle and knee joints of the exoskeleton. Applying the eqs. (7), (8), and (9), the connectivities (l_1, l_2) are determined to be $(5, 5)$.

2.2 Brace Design

The proposed brace was designed to transmit the forces along the desired axis of motion while suppressing parasitic forces along the other axes as previously outlined. While achieving this goal, a special emphasis was given to contain the size and weight of the brace structure for enhanced comfort [32, 33].

To this end, the brace is modeled as displayed in Fig. 3. Points H, K, and D represent the exoskeleton hip joint, exoskeleton knee joint, and the contact point between the human limb and brace. The link HK represents the exoskeleton thigh. Segments AB, BC, and CD represent the links between the exoskeleton and human thigh, with lengths l_{AB}, l_{BC}, and l_{CD}, respectively. The robot exerts the torque τ at point H along the x-direction. The symbols τ_{Dx}, f_{Dy}, and f_{Dz} denote the moment and forces exerted at the point D in x, y, and z directions, respectively. To achieve the desired design objectives, it is necessary to eliminate f_{Dz} (indicated by the red arrow), minimize τ_{Dx} (indicated by the green arrow at point D), and maximize the force f_{Dy} (indicated by the orange arrow).

Observing Fig. 3, the interaction force components $(\tau_{Dx}, f_{Dy}, f_{Dz})$ could be mapped to the robot torque τ as follows:

$$\tau = \tau_{Dx} + f_{Dy} l_{HA} - f_{Dz}(l_{AB} - l_{CD}), \qquad (10)$$

where l_{HA} is the length of the segment HA. Based on (10), we conclude the following: (i) the moment τ_{Dx} can be eliminated by introducing a passive revolute joint along its axis, thereby preventing stress on the human tissues; (ii) the force f_{Dy} needs to be increased, but the contact area should be sufficiently large to reduce the applied pressure on the human body; and (iii) the force f_{Dz} can be minimized by incorporating a passive linear joint along its axis of application, which helps avoid hyperstatic forces that might otherwise act tangentially against the human skin. The length l_{HA} is selected to ensure user comfort, while the segment $l_{AB} - l_{CD}$ is minimized to reduce any residual forces arising from the vertical force component f_{Dz}.

Additionally, two more degrees of freedom (DOF) were added at point D based on the model presented in [27]. Rotations about the z and y axes were permitted to alleviate tangential and torsional stresses on human tissues. To achieve the five DoF for each brace as outlined in Section 2.1, it would be necessary to release the translation constraint of the brace in the x-direction. However, given that the exoskeleton could exhibit minimal lateral motion due to its actuated joint configuration, we chose to utilize only the four available DOF instead, thereby minimizing manufacturing complexity and improving economic efficiency. Key design parameters, such as the length and weight of parts, were tuned via a parametric analysis [34]. While this analysis has focused solely on the design of the thigh brace, a similar approach can be applied to the design of the shank brace.

2.2.1 *Stress Analysis*

The proposed brace must be lightweight yet sufficiently durable. To evaluate this, the brace structure was analyzed under static loading with its passive joints fixed. A Finite Element Analysis (FEA) was performed using ANSYS Workbench. The analysis simulated an equivalent force corresponding to a sit-to-stand motion exerted by a passive user weighing 75 kg. For stress analysis, a force of 375 N, approximately half of the user's weight, was applied to the inner cuff along the y-axis; see Fig. 4. The ANSYS software generated a mesh with 2,313,808 nodes and 605,209 elements to compute the corresponding von Mises stress values. Fig. 4 illustrates the stress distributions across all components of the designed brace.

The material selection was guided by the FEA results to ensure structural safety under expected loading. Parts A and E are made of carbon-reinforced Onyx, which has a tensile strength of 566 MPa; Parts B and D are made of aluminum 6061, with a tensile strength of 496 MPa; and Part C is made of ABS, with a tensile strength of 32 MPa [35, 36, 37]. The analysis results indicate that Link B experiences the highest stress, reaching 248 MPa, as shown in Fig. 4. The cuff was designed with a wide structure to reduce stress on the human limb, and soft, ergonomic materials such as polypropylene were used to enhance comfort.

2.2.2 *Simulation Experiment*

In order to test the effectiveness of the proposed design approach for the brace, a human-robot coupled model was constructed using MSC ADAMS [38]. This model combined an anthropomorphic human model weighing 75 kg and measuring 180 cm in length with a realistic model of our self-balancing exoskeleton, named Co-Ex [25]; see Fig. 5. The human-robot fixation points were configured to satisfy the connectivity conditions de-

rived above. For comparison, another model was constructed using the conventional approach, where the fixation points did not include any passive additional DOFs. Both models were tested using smooth stand-to-sit and sit-to-stand trajectories within the MSC ADAMS/MATLAB Simulink co-simulation environment [39].

The variations in interaction forces between the brace and the human thigh are shown in Fig. 6. In this figure, the solid blue and dashed red lines represent interaction forces along the y and z axes (F_y, F_z), as well as the interaction moment about the x axis (τ_x). Given that the stand-sit-stand motion occurs predominantly within the sagittal y-z plane (see Fig. 4), we analyze these components of the interaction force and moments. During the target motion, F_y is the force to be transmitted to human model, whereas F_z and τ_x are parasitic interaction forces to be minimized.

The simulation begins with the combined human-robot model in a standing position, followed by a transition to the sit-to-stand phase, then to a sitting phase, another sit-to-stand transition, and finally back to a standing posture. For the case of conventional brace, F_z and τ_x maintained a value of 200 N and 50 Nm, respectively, during the sitting phase. They also showed greater peak values; 500 N for F_z and 75 Nm for τ_x. On the contrary, the proposed brace was able to minimize these undesired interaction force and moment, as they maintain a value around 0.

The proposed brace design reduces the maximum interaction force along the y-axis to 108 N during the stand-to-sit and sit-to-stand phases, maintaining this value during the sitting phase. In contrast, conventional braces exhibited a significantly higher interaction force of approximately 275 N. This reduction is attributed to the mitigation of reactive forces and torques caused by the misalignment between the centers of rotation of the exoskeleton link and the human limb. Specifically, the reactive torque generated in conventional designs increases the supporting force component, leading to higher transmitted forces. These additional forces ensure that the passive human model achieves the desired sit-to-stand motion, albeit at the cost of increased interaction forces.

Furthermore, Fig. 7, displays the human model's hip flexion/extension, knee flexion/extension, and ankle dorsi/plantar flexion joints' variations for both cases. As depicted in this figure, human model joints followed similar trajectories in both brace types, the maximum differences are 3.23^o, 6.33^o, 7.65^o, respectively. These results effectively demonstrate that the similar stand-to-sit and sit-to-stand trajectories are realized in both cases, suggesting that the proposed brace does not alter the target motion characteristic.

The simulation results demonstrated strong potential for the proposed approach, showing that the brace could adjust its posture passively. This capability led to a significant reduction in the resultant interaction force. Consequently, the identified connectivities, and the configuration of additional passive DOFs for the brace, are validated.

2.3 Hardware Assembly

2.3.1 Manufacturing of the Proposed Brace

The CAD model of the assembled brace hardware components is shown in Fig. 8. The brace features three rotational degrees of freedom along the x, y, and z axes and one translational degree of freedom along the z-axis, as indicated by the blue motion arrows in Fig. 8. This design incorporates passive DoFs to minimize parasitic forces caused by misalignments between the human and exoskeleton joints, while also ensuring user comfort and safety.

The brace structure is supported by a *Linear Guide*, which enables passive linear motion along the z-axis to accommodate vertical misalignments. A rod (*Link 1*) connected to the linear guide serves as the base for the rotational motion of *Connector 2*. *Connector 2*, supported by rolling bearings at the free end of *Link 1*, provides rotational freedom around the y-axis to compensate for angular misalignments. *Link 2* connects to *Connector 3*, which offers rotational freedom around the x-axis and also functions as a curved guide, allowing the cuff to rotate about the z-axis relative to *Connector 3*. Adjustable plastic collars and nuts are incorporated to ensure proper fit, secure the components, and prevent separation during use.

During operation, the linear guide adapts to vertical movements, while *Connector 2* ensures angular alignment along the y-axis. *Connector 3* provides additional rotational flexibility along the x- and z-axes, enabling the brace to follow the user's natural motion. Additionally, the design includes a quick detachment mechanism to enhance safety in unforeseen situations.

Fig. 9 presents the manufactured brace hardware assembly. Fig. 9.a shows the brace as a standalone component, while Fig. 9.b illustrates the brace attached to the exoskeleton thigh. The proposed brace design is constructed using lightweight composite materials, including micro carbon fiber-filled nylon (Onyx, Markforged Corp, Waltham, MA.), ABS (Ultimaker B.V., Geldermalsen, the Netherlands), and space-grade aluminum. Despite the addition of a quick-release solenoid attachment, the total weight of the proposed brace is 869 grams, which is only 220 grams more compared to the fixed brace design.

2.3.2 Sensor Deployment

To collect in-situ measurements at the brace contact, we utilized **Force Sensing Resistor (FSR)** (Interlink Electronics FSR UX 402, Irvine, CA, US) elements due to its favorable characteristics when properly calibrated [40]. To properly measure force, FSR elements must be attached to rigid surfaces. To this end, we manufactured a segmented watch strap-like mechanism (see Fig. 10) made from carbon fiber-filled nylon (Onyx, Markforged Corp, Waltham, MA.) and deployed an FSR in each segment [30], making it a total of 7 FSRs. Thin plastic cylindrical parts were used to concentrate the load on the FSR's active area. The top view of the FSRs, cuff, brace, dummy thigh, and exoskeleton thigh installation are shown in Fig. 11. The FSRs are indicated by light blue circles. The strap is tightened uniformly to ensure that all FSRs measure at least 10% of its maximum value. Compared to existing solutions, e.g., [41], we were able to deploy in-situ measurement sensors which are tightly integrated within the brace such that the mobility is not adversely effected.

In addition to the force measurement, the brace center of pressure (COP) and its translocation velocity were obtained to evaluate how the forces aligned with the parasitic axis and the contact stability. The COP results are represented as an angle measured counterclockwise (CCW) from the x-axis, with the CCW direction defined as positive and the clockwise (CW) direction as negative, following the convention in [42].

3 EXPERIMENT RESULTS AND DISCUSSION

3.1 Experimental Setup

The self-balancing lower limb exoskeleton Co-Ex was built in our laboratory [25] and it was used as the experimental testbed in this study. The exoskeleton has 8 torque-controllable active joints and it can perform various motion profiles. In normal operation, it is equipped with conventionally designed braces.

To provide thorough results, we used the Co-Ex left thigh brace as a baseline. We focused on the left thigh brace, as similar results could be obtained from the other braces. In one set of experiments, the conventional brace was utilized. Subsequently, the same set of experiments was conducted using identical motion profiles, but this time with the proposed brace installed as the left thigh brace. Two lower-body dummies with different weights were used to simulate human leg limbs: a lighter dummy weighing approximately $6\ kg$ and a heavier dummy weighing around $35\ kg$. Fig. 12 shows the lighter dummy connected to Co-Ex links. The dashed lines represent the rotation axes of the exoskeleton and dummy knee joints, illustrating the misalignment between the Co-Ex and dummy joint rotation axes.

3.2 Experimental Results and Discussion

A set of 34 experiments was conducted for each dummy, involving two different motion patterns: squatting and swaying. The squatting motion included two different amplitudes, 3.5 cm, and 5 cm, for vertical torso displacement across four frequencies ranging from 0.2 Hz to 0.5 Hz. The swaying motion was performed at 0.25 Hz, 0.33 Hz, and 0.5 Hz, with three torso-to-vertical axis roll angles of 4°, 6°, and 7°. All motion profiles were executed for both the conventional and proposed braces using both the heavier and lighter dummies. Note that self-balancing walking experiments were not feasible due to unavoidable low structural stiffness [43].

A segmented strap mechanism incorporating FSRs was used to enable in-situ force measurements at the brace contact while maintaining mobility. Uniform load distribution and accurate data collection were achieved, offering improved integration and functionality compared to existing solutions [41].

Fig. 13 illustrates the force variations measured on the dummy's left thigh for both the conventional and proposed braces. Fig. 13.a and 13.c display the forces recorded during squatting and swaying experiments with the heavier dummy. Fig. 13.b and 13.d show the forces for the same experiments using the lighter dummy. The solid lines represent the mean values, while the shaded regions indicate the standard deviation (SD). Red lines correspond to the conventional brace, and blue lines represent the proposed brace data.

For both the squatting and swaying experiments, the conventional brace exerts significantly higher forces on the dummy's thigh compared to the proposed brace. Additionally, the force exerted by the conventional brace exhibits greater fluctuations during motion. These fluctuations arise because all degrees of freedom in the conventional brace are restricted relative to the dummy's leg, causing the leg to slide along the brace during movement. This sliding results in measurement variations, particularly due to the non-uniform cylindrical shape of the dummy's leg and the brace, which introduces parasitic forces. In contrast, the proposed brace offers additional degrees of freedom, which help minimize slippage between the dummy's leg and the brace. Consequently, the proposed brace's ability to adapt its posture passively to the exoskeleton's motion results in a significant reduction in parasitic forces.

Numerically, using the proposed brace resulted in significant reductions in both the average force and peak-to-peak values. Specifically, for the squatting experiments with the heavy dummy, the average force and peak-to-peak values decreased by

16.22% and 77.96%, respectively. For the swaying experiments with the heavy dummy, these values decreased by 15.21% and 72.61%. For the squatting experiments with the light dummy, reductions were 14.74% and 69.31%, while for the swaying experiments with the light dummy, reductions were 13.41% and 46.93%. These numerical results highlight the significant impact of the proposed brace on reducing parasitic forces. The substantial reduction is likely due to the elimination of slippage between the dummy limb and the proposed brace, facilitated by its passive joints.

Since contact forces are measured using an array of distributed FSRs, we can compute the center of pressure (COP). In biomechanics literature, COP is a crucial indicator of postural stability, and higher variations in COP are considered a negative indicator of postural stability due to improper contact [44, 42]. Therefore, we collected COP data using in-situ measurements and assessed contact stability based on its variation, specifically its first time derivative. Fig. 14.a and 14.c display the COP variations for the heavy dummy during squatting and swaying experiments, respectively, while Fig. 14.b and 14.d show the variations for the light dummy experiments. The solid lines indicate the mean values, and the shaded regions represent the standard deviation. Red lines represent the COP data for the conventional brace, while blue lines represent the COP data for the proposed brace. The results indicate that the proposed brace reduces COP oscillations compared to the conventional brace. The peak-to-peak values of the average signals shown in Fig. 14 are reduced by 80.31% and 72.75% for squatting and swaying with the heavy dummy, respectively, and by 74.1% and 26.94% for squatting and swaying with the light dummy.

The variation in the rate of change of COP, denoted by ΔCOP, is shown in Fig. 15. The ΔCOP variation for the heavy dummy during squatting and swaying experiments is depicted in Fig. 15.a and Fig. 15.c, respectively. Fig. 15.b and Fig. 15.d illustrate the ΔCOP variation for the light dummy during squatting and swaying experiments, respectively. The solid red and blue lines represent the mean ΔCOP values for the conventional and proposed braces, respectively. The results show a significantly larger ΔCOP variation for the conventional brace compared to the proposed brace, indicating less slippage between the proposed brace and the dummy limb. Consequently, the peak-to-peak values for the heavy dummy during squatting and swaying experiments are reduced by 69.06% and 49.85%, respectively, with the proposed brace. For the light dummy, the reductions are 90.26% and 50.40%, respectively. These results demonstrate that the proposed brace significantly reduces slippage between the brace and the dummy thigh.

3.3 Statistical Analysis

We statistically analyzed the results presented in the previous subsections to determine whether the proposed brace provides statistically significant improvements compared to the conventional brace. We used eight datasets, with each dataset containing data from eight experiments. Each dataset was obtained using either a heavy or light dummy, during either squatting or swaying motions, and with either the conventional or proposed brace. To define metrics, we measured the average brace force and the peak-to-peak values of COP and ΔCOP for each experiment.

Analysis of variance was performed using Repeated Measures ANOVA to test the significant difference between braces for both dummies. We used the MATLAB function *ranova(•)* at a significance level of 0.05. There was a significant difference between the braces for the heavy dummy, $F(1,7) = 45.2630, p = 0.0003$, and for the light dummy, $F(1,7) = 6.2895, p = 0.0405$.

Afterward, a post-hoc test was conducted using Bonferroni correction with an adjusted significance level of 0.0167 per test (0.05/3). The MATLAB function *multcompare(•)* was used, and the results were displayed in Table 1. The analysis revealed a significant reduction in average metrics values when proposed brace $(M = 11.5985, SD = 6.7682)$ was used, compared to conventional brace $(M = 14.8831, SD = 4.4790)$ for the case of heavy dummy. Regarding the light dummy, the metrics values are significantly lower when the proposed brace $(M = 12.3296, SD = 2.0071)$ was used, compared to conventional brace $(M = 21.6751, SD = 55.0660)$. The p-Value and t-Value parameters for each pairwise comparison are reported in Table 1, columns 4 and 5, respectively.

The second and third columns show the mean difference, $\Delta\mu$, and mean squared error, σ^2_Δ, of the two braces in comparison. The last two columns display the 95% confidence interval (CI) for the mean difference between the two braces. The results indicate that the proposed brace is statistically more favorable compared to the conventional brace concerning both dummies. Furthermore, Fig. 16 and 17 illustrate the variation between the two braces based on the averages of the three metrics for heavy and light dummies, respectively. Similarly, the proposed brace provided less variation when compared to the conventional brace.

3.4 Limitations

The primary limitation of this study is the absence of human-involved experiments, due to the

Dummy	$\Delta\mu = \overline{CB} - \overline{PB}$	σ^2_Δ	p-Value	t-Value	95% CI	
					Lower bound	Upper bound
Heavy Dummy	3.6891	7.2162	0.0003	4.7801	2.3925	4.9857
Light Dummy	9.3455	333.27	0.0405	2.5079	0.5338	18.1570

Table 1: Statistical significance among the two braces designs. The symbols $\overline{CB}$ and $\overline{PB}$ indicate the conventional and proposed brace mean values.

ongoing verification of the safety layer for the lower-body exoskeleton Co-Ex. Instead, we employed dummy manikins with varying masses and mass distributions to simulate the passive response of spinal cord injury users to the exoskeleton's motions. This methodology provides valid results and is applicable to future studies involving human subjects.

Although the results demonstrate the functionality of the proposed brace, its actual performance with human subjects remains to be validated. To address this limitation, we are developing experimental protocols for human trials involving the Co-Ex exoskeleton. Results from these human-involved experiments and clinical evaluations will be reported in future work.

4 CONCLUSION

This paper presented a novel brace design approach incorporating passive degrees of freedom to minimize parasitic forces and enhance contact stability. Structural analysis, through static and dynamic simulations, demonstrated its capacity to withstand expected stresses. The dynamic analysis revealed that integrating passive degrees of freedom effectively reduces the forces exerted on the user.

Statistical analysis of the experimental results, including ANOVA tests, confirmed significant improvements with the brace featuring passive degrees of freedom compared to the conventional brace. The Center of Pressure (CoP) analysis highlighted the enhanced performance of the proposed brace, as it effectively minimized parasitic forces whilst maintaining contact stability, thus potentially increasing comfort [20].

The proposed brace design with passive joints adds minimal complexity compared to a traditional brace, while significantly enhancing alignment with human movement and offering greater comfort. This design choice is justified by both theoretical and experimental analysis, demonstrating that the benefits outweigh the complexity, making it a practical solution for exoskeleton applications.

While previous studies have explored the use of passive DoFs in upper-body exoskeletons to address misalignment forces [26, 27], these approaches have not been extended to lower-body applications. Lower-body exoskeletons present unique challenges due to the higher interaction forces and the need for alignment during activities like walking and sit-to-stand transitions. While parasitic force reduction in lower-limb exoskeletons has been addressed through control-based strategies [45], joint-level self-alignment mechanisms [46], and flexible structures [47], a systematic mechanical design approach that introduces passive degrees of freedom at the brace level to reduce parasitic forces has not yet been explored. To the best of our knowledge, this study is the first to implement and evaluate such an approach in a lower-body exoskeleton design.

Overall, these findings demonstrate the efficacy of the proposed brace design approach compared to the conventional approach, addressing a critical gap in the existing literature. The implications for future exoskeleton and assistive device development are significant, suggesting improvements in user safety and reductions in discomfort or skin-related issues caused by excessive forces during movement. The proposed brace may be applied to other exoskeletons and evaluated with human participants in future works, and has been tested under gait-like joint trajectories to assess its performance in continuous motion tasks.

ACKNOWLEDGEMENTS

This work was supported by the Scientific and Technological Research Council of Türkiye (TUBITAK) under Grant No. 118E922.

REFERENCES

[1] Zoss, A. B., Kazerooni, H., and Chu, A., 2006, "Biomechanical design of the berkeley lower extremity exoskeleton (BLEEX)," *IEEE/ASME Trans. Mechatronics,* **11**(2), Apr., pp. 128–138.

[2] Young, A. J., and Ferris, D. P., 2017, "State of the art and future directions for lower limb robotic exoskeletons," *IEEE Trans. Neural Syst. Rehabil. Eng.,* **25**(2), Feb., pp. 171–182.

[3] Zeilig, G., Weingarden, H., Zwecker, M., Dudkiewicz, I., Bloch, A., and Esquenazi, A., 2012, "Safety and tolerance of the ReWalk$^{(TM)}$ exoskeleton suit for ambulation by people with complete spinal cord injury: A pilot study," *J. Spinal Cord Med.,* **35**, Feb., pp. 96–101.

[4] Font-Llagunes, J. M., Lugrís, U., Clos, D., Alonso, F. J., and Cuadrado, J., 2020, "Design, Control, and Pilot Study of a Lightweight and Modular Robotic Exoskeleton for Walking Assistance After Spinal Cord Injury," *Journal of Mechanisms and Robotics,* **12**(3), 01, p. 031008.

[5] Lajeunesse, V., Vincent, C., Routhier, F., Careau, E., and Michaud, F., 2015, "Exoskeletons design and usefulness evidence according to a systematic review of lower limb exoskeletons used for functional mobility by people with spinal cord injury," *Disability and Rehabilitation: Assistive Technology,* **11**(7), Sept., pp. 535–547.

[6] Baltrusch, S. J., Houdijk, H., van Dieën, J. H., van Bennekom, C. A. M., and de Kruif, A. J. T. C. M., 2020, "Perspectives of end users on the potential use of trunk exoskeletons for people with low-back pain: A focus group study," *Human Factors: The Journal of the Human Factors and Ergonomics Society,* **62**(3), Jan., pp. 365–376.

[7] Cheng, C. Y. M., Lee, C. C. Y., Chen, C. K., and Lou, V. W. Q., 2022, "Multidisciplinary collaboration on exoskeleton development adopting user-centered design: a systematic integrative review," *Disability and Rehabilitation: Assistive Technology,* **19**(3), Oct., pp. 909–937.

[8] Siviy, C., Baker, L. M., Quinlivan, B. T., Porciuncula, F., Swaminathan, K., Awad, L. N., and Walsh, C. J., 2022, "Opportunities and challenges in the development of exoskeletons for locomotor assistance," *Nature Biomedical Engineering,* **7**(4), Dec., pp. 456–472.

[9] Babic, J., Laffranchi, M., Tessari, F., Verstraten, T., Novak, D., Sarabon, N., Ugurlu, B., Peternel, L., Torricelli, D., and Veneman, J. F., 2021, "Challenges and solutions for application and wider adoption of wearable robots," *Wearable Technologies,* **2**, Nov.

[10] Ergin, M. A., and Patoglu, V., 2011, "A self-adjusting knee exoskeleton for robot-assisted treatment of knee injuries," In 2011 IEEE/RSJ International Conference on Intelligent Robots and Systems, IEEE.

[11] Zanotto, D., Akiyama, Y., Stegall, P., and Agrawal, S. K., 2015, "Knee joint misalignment in exoskeletons for the lower extremities: Effects on user's gait," *IEEE Trans. Robot.,* **31**(4), Dec., pp. 978–987.

[12] Bartenbach, V., 2017, "Constraints caused by lower extremity exoskeletons," PhD thesis, ETH Zurich, Zurich, Switzerland, Jan.

[13] Esquenazi, A., Talaty, M., Packel, A., and Saulino, M., 2012, "The rewalk powered exoskeleton to restore ambulatory function to individuals with thoracic-level motor-complete spinal cord injury," *American Journal of Physical Medicine & Rehabilitation,* **91**, Nov., pp. 911–21.

[14] Colombo, G., Jörg, M., Schreier, R., and Dietz, V., 2000, "Treadmill training of paraplegic patients using a robotic orthosis.," *J. Rehabil. Res. Dev.,* **37 6**, Nov., pp. 693–700.

[15] Pablo, D., Clarissa, R., and Yimesker, Y., 2022, "Human-exoskeleton joint coordination assessment: A case study on the shoulder and elbow joints," *Journal of Bionic Engineering,* **19**(6), pp. 1712–1721.

[16] Shafiei, M., and Behzadipour, S., 2019, "The Effects of the Connection Stiffness of Robotic Exoskeletons on the Gait Quality and Comfort," *Journal of Mechanisms and Robotics,* **12**(1), 10, p. 011007.

[17] Wang, J., Li, X., Huang, T., Yu, S., Li, Y., Chen, T., Carriero, A., Oh-Park, M., and Su, H., 2018, "Comfort-centered design of a lightweight and backdrivable knee exoskeleton," *IEEE Robot. Autom. Lett.,* **3**(4), Oct., pp. 4265–4272.

[18] Beil, J., Marquardt, C., and Asfour, T., 2017, "Self-aligning exoskeleton hip joint: Kinematic design with five revolute, three prismatic and one ball joint," In Procs. IEEE Int. Conf. Rehabil. Robot. (ICORR), pp. 1349–1355.

[19] Junius, K., Degelaen, M., Lefeber, N., Swinnen, E., Vanderborght, B., and Lefeber, D., 2017, "Bilateral, misalignment-compensating, full-dof hip exoskeleton: Design and kinematic validation," *Applied Bionics and Biomechanics,* **2017**, July, pp. 1–14.

[20] Sarkisian, S., Ishmael, M., and Lenzi, T., 2021, "Self-aligning mechanism improves comfort and performance with a powered knee exoskeleton," *IEEE Transactions on Neural Systems and Rehabilitation Engineering,* **29**, Mar., pp. 629–640.

[21] Zimmermann, Y., Song, J., Deguelle, C., Laderach, J., Zhou, L., Hutter, M., Riener, R., and Wolf, P., 2023, "Humanrobot attachment system for exoskeletons: Design and performance analysis," *IEEE Transactions on Robotics,* **39**(4), Aug., pp. 3087–3105.

[22] Awad, M. I., Hussain, I., Ghosh, S., Zweiri, Y., and Gan, D., 2020, "A Double-Layered Elbow Exoskeleton Interface With 3-PRR Planar Parallel Mechanism for Axis Self-Alignment," *Journal of Mechanisms and Robotics,* **13**(1), 11,

p. 011016.
[23] Stienen, A. H. A., Hekman, E. E. G., van der Helm, F. C. T., and van der Kooij, H., 2009, "Self-aligning exoskeleton axes through decoupling of joint rotations and translations," *IEEE Transactions on Robotics,* **25**(3), pp. 628–633.
[24] Lee, B., Lee, S., and Han, C.-s., 2020, "Design of fixations for an exoskeleton device with joint axis misalignments," *Int. J. Precis. Eng. Manufac.,* **21**, June.
[25] Soliman, A. F., Coruk, S., Yildirim, M. C., Ugur, D., Cevik, S. C., Ozkaynak, B., Sendur, P., and Ugurlu, B., 2024, "Design, development, and control for the self- stabilizing bipedal exoskeleton prototype co-ex," *IEEE/ASME Transactions on Mechatronics*, pp. 1–11.
[26] Lee, B., Lee, S. C., and Han, C.-s., 2020, "Design of fixations for an exoskeleton device with joint axis misalignments," *International Journal of Precision Engineering and Manufacturing,* **21**(7), June, pp. 1291–1298.
[27] Jarrasse, N., and Morel, G., 2012, "Connecting a human limb to an exoskeleton," *IEEE Transactions on Robotics,* **28**(3), June, pp. 697–709.
[28] Kerdraon, J., Previnaire, J. G., Tucker, M., Coignard, P., Allegre, W., Knappen, E., and Ames, A., 2021, "Evaluation of safety and performance of the self balancing walking system atalante in patients with complete motor spinal cord injury," *Spinal Cord Series and Cases,* **7**(1), Aug.
[29] Meijneke, C., van Oort, G., Sluiter, V., van Asseldonk, E., Tagliamonte, N. L., Tamburella, F., Pisotta, I., Masciullo, M., Arquilla, M., Molinari, M., Wu, A. R., Dzeladini, F., Ijspeert, A. J., and van der Kooij, H., 2021, "Symbitron exoskeleton: Design, control, and evaluation of a modular exoskeleton for incomplete and complete spinal cord injured individuals," *IEEE Transactions on Neural Systems and Rehabilitation Engineering,* **29**, pp. 330–339.
[30] Coruk, S., 2021, "Development of a torque-controllable upper limb exoskeleton for industrial applications," Master's thesis, Özyeğin University, Istanbul, TR.
[31] Waldron, K., 1966, "The constraint analysis of mechanisms," *J. Mechanisms,* **1**(2), June, pp. 101–114.
[32] Crowell, P., 1995, Chuman engineering design guidelines for a powered, full body exoskeleton Tech. Rep. ARL-TN-60, US Army Research Lab, Aberdeen Proving Ground, Maryland, July.
[33] Levesque, L., Pardoel, S., Lovrenovic, Z., and Doumit, M., 2017, "Experimental comfort assessment of an active exoskeleton interface," In 2017 IEEE International Symposium on Robotics and Intelligent Sensors (IRIS), pp. 38–43.
[34] Cevik, S. C., Derman, M., Unal, R., Ugurlu, B., and Bebek, O., 2021, "A custom brace design to connect a user limb to an exoskeleton link with minimal discomfort," In 2021 IEEE 19th International Conference on Industrial Informatics (INDIN), pp. 1–6.
[35] Parmiggiani, A., Prato, M., and Pizzorni, M., 2021, "Effect of the fiber orientation on the tensile and flexural behavior of continuous carbon fiber composites made via fused filament fabrication," *The International Journal of Advanced Manufacturing Technology,* **114**, pp. 2085–2101.
[36] Li, J., Jia, Y., Li, T., Zhu, Z., Zhou, H., Peng, X., and Jiang, S., 2020, "Tensile behavior of acrylonitrile butadiene styrene at different temperatures," *Advances in Polymer Technology,* **2020**, 04, pp. 1–10.
[37] Bobruk, E. V., Dolzhenko, P. D., Murashkin, M. Y., Valiev, R. Z., and Enikeev, N. A., 2022, "The microstructure and strength of ufg 6060 alloy after superplastic deformation at a lower homologous temperature," *Materials,* **15**(19).
[38] Angel, L., Pérez, M., Díaz-Quintero, C., and Mendoza, C., 2012, "Adams/matlab co-simulation: Dynamic systems analysis and control tool," *Applied Mechanics and Materials,* **232**, Nov., pp. 527–531.
[39] Derman, M., Soliman, A. F., Kuru, A., Cevik, S. C., Unal, R., Bebek, O., and Ugurlu, B., 2022, "Simulation-based design and locomotion control implementation for a lower body exoskeleton," In 2022 IEEE 5th International Conference on Industrial Cyber-Physical Systems (ICPS), IEEE.
[40] Lebosse, C., Renaud, P., Bayle, B., and de Mathelin, M., 2011, "Modeling and evaluation of low-cost force sensors," *IEEE Transactions on Robotics,* **27**(4), Aug., p. 815822.
[41] McCann, C. M., Hohimer, C. J., ONeill, C. T., Young, H. T., Bertoldi, K., and Walsh, C. J., 2023, "In-situ measurement of multi-axis torques applied by wearable soft robots for shoulder assistance," *IEEE Transactions on Medical Robotics and Bionics,* **5**(2), May, pp. 363–374.
[42] Clark, S., and Riley, M. A., 2006, "Multisensory information for postural control: sway-referencing gain shapes center of pressure variability and temporal dynamics," *Experimental Brain Research,* **176**(2), July, p. 299310.
[43] Vigne, M., Khoury, A. E., Di Meglio, F., and Petit, N., 2020, "Improving low-level control of the exoskeleton atalante in single support by compensating joint flexibility," In 2020 IEEE/RSJ International Conference on Intelligent Robots

and Systems (IROS), IEEE, pp. 3437–3443.
[44] Taveira, H. V., de Lira, C. A. B., Andrade, M. S., Viana, R. B., Tanaka, H., Hill, L., Nikolaidis, P. T., Knechtle, B., Rosemann, T., and Vancini, R. L., 2021, "Isokinetic muscle strength and postural sway of recreationally active older adults vs. master road runners," *Frontiers in Physiology,* **12**, Mar.
[45] Zhou, L., Chen, W., Bai, S., Wang, J., Zhao, Z., Zhao, X., and Yu, X., 2022, "Lower limb exoskeleton parasitic force modeling and minimizing with an adaptive trajectory controller," *Mechanism and Machine Theory,* **170**, Apr., p. 104731.
[46] Celebi, B., Yalcin, M., and Patoglu, V., 2013, "Assiston-knee: A self-aligning knee exoskeleton," In 2013 IEEE/RSJ International Conference on Intelligent Robots and Systems, pp. 996–1002.
[47] Lee, Y., Kim, Y.-J., Lee, J., Lee, M., Choi, B., Kim, J., Park, Y. J., and Choi, J., 2017, "Biomechanical design of a novel flexible exoskeleton for lower extremities," *IEEE/ASME Transactions on Mechatronics,* **22**(5), pp. 2058–2069.

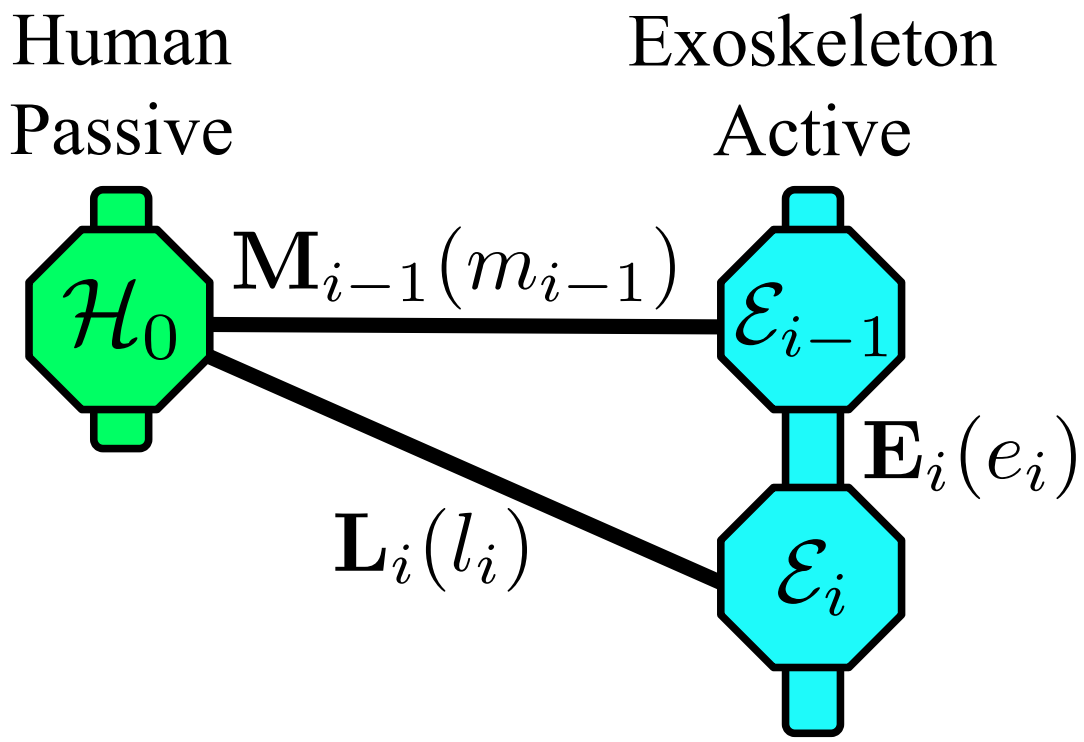


Fig. 1: The simplified connection model consists of an exoskeleton leg and a human leg and the fixations in between them.

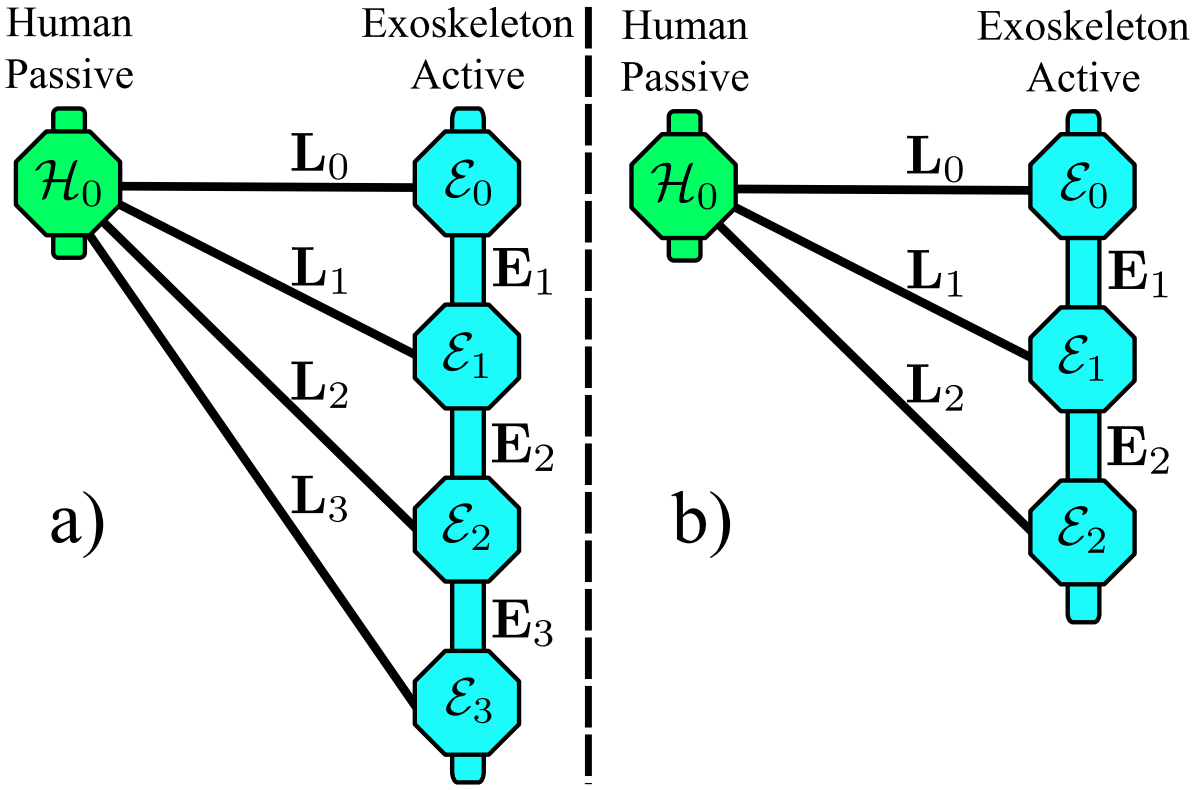


Fig. 2: The simplified connection model between the CoEx leg and the human leg in a static posture. a) Fixed torso schematic connection. b) Fixed foot schematic connection.

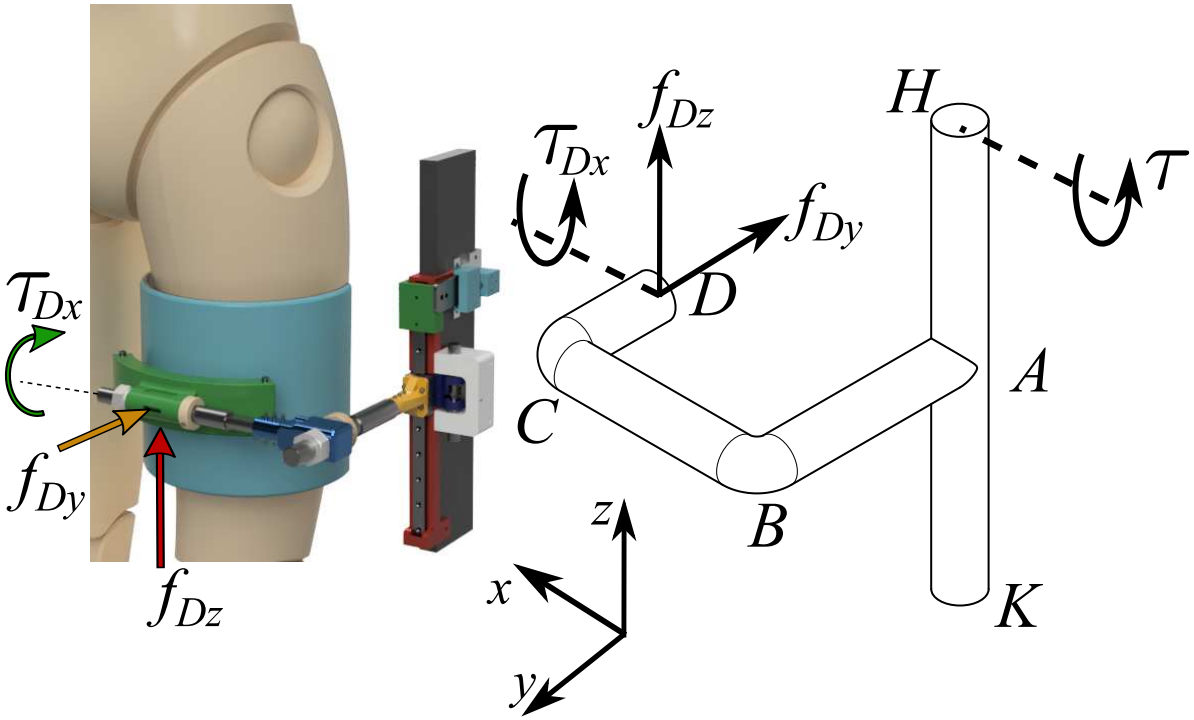


Fig. 3: The proposed brace, connected to a human model with its equivalent free-body diagram.

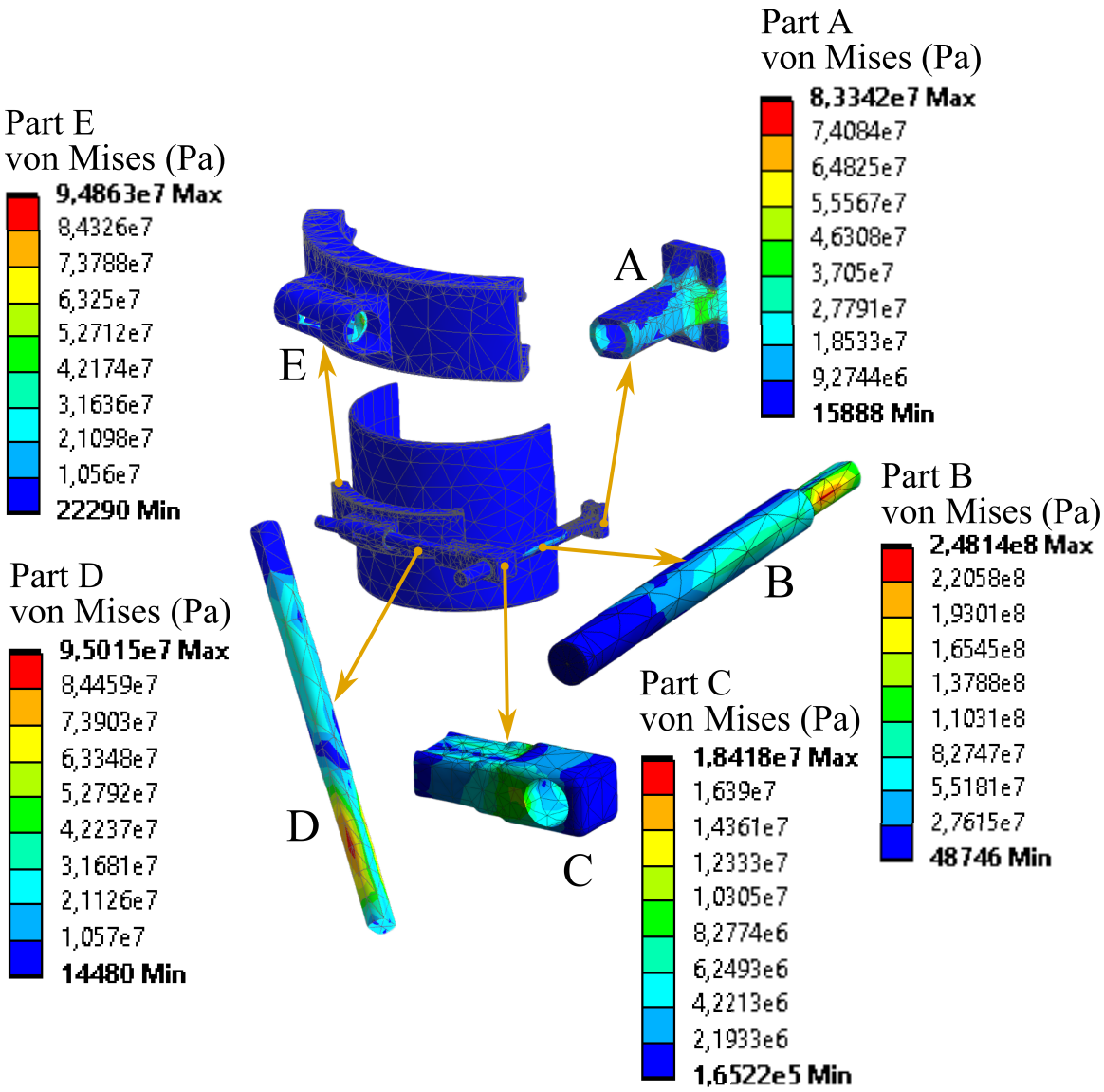


Fig. 4: The stress distribution over the proposed brace parts.

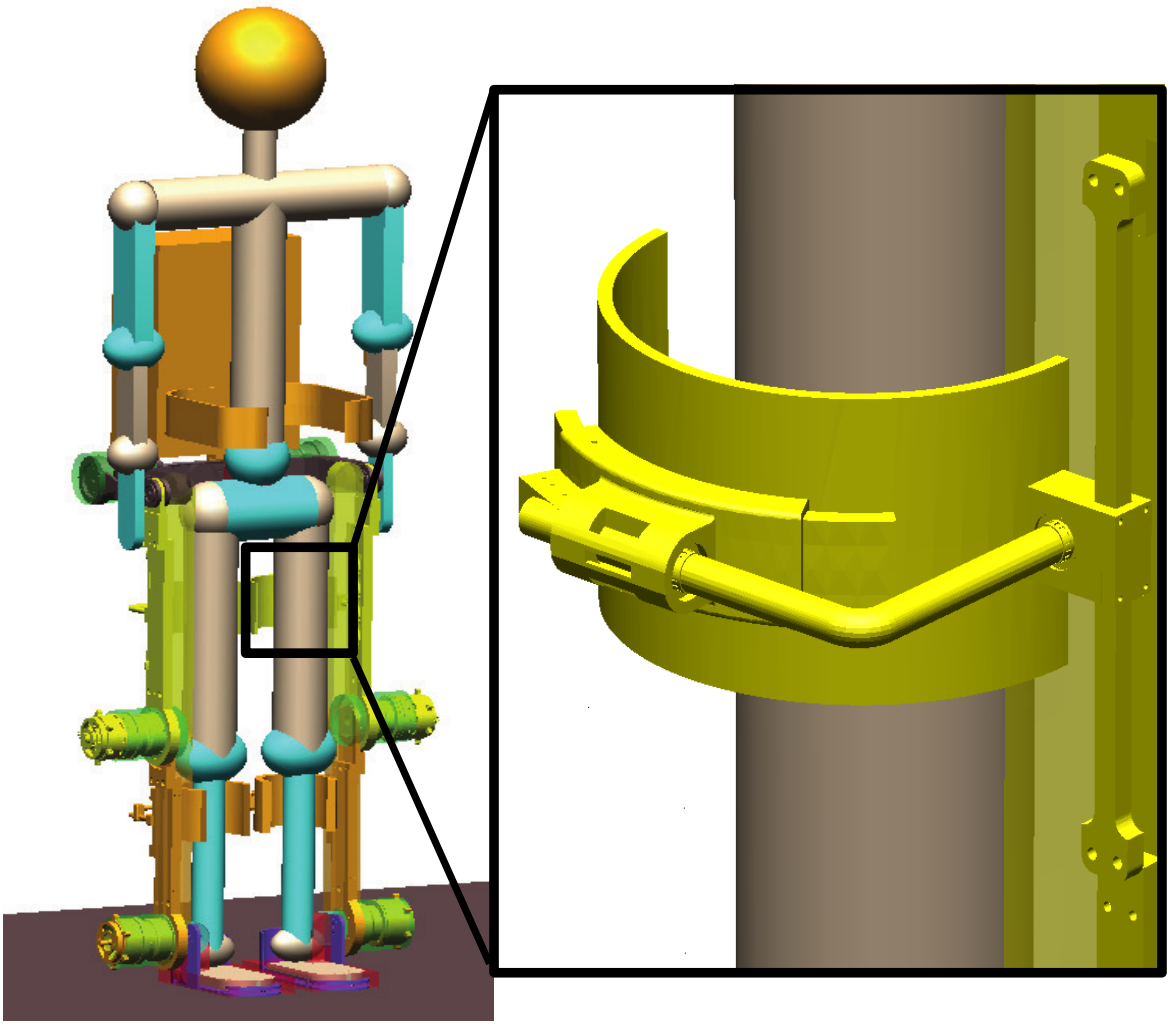


Fig. 5: MSC ADAMS model used in the simulation experiments.

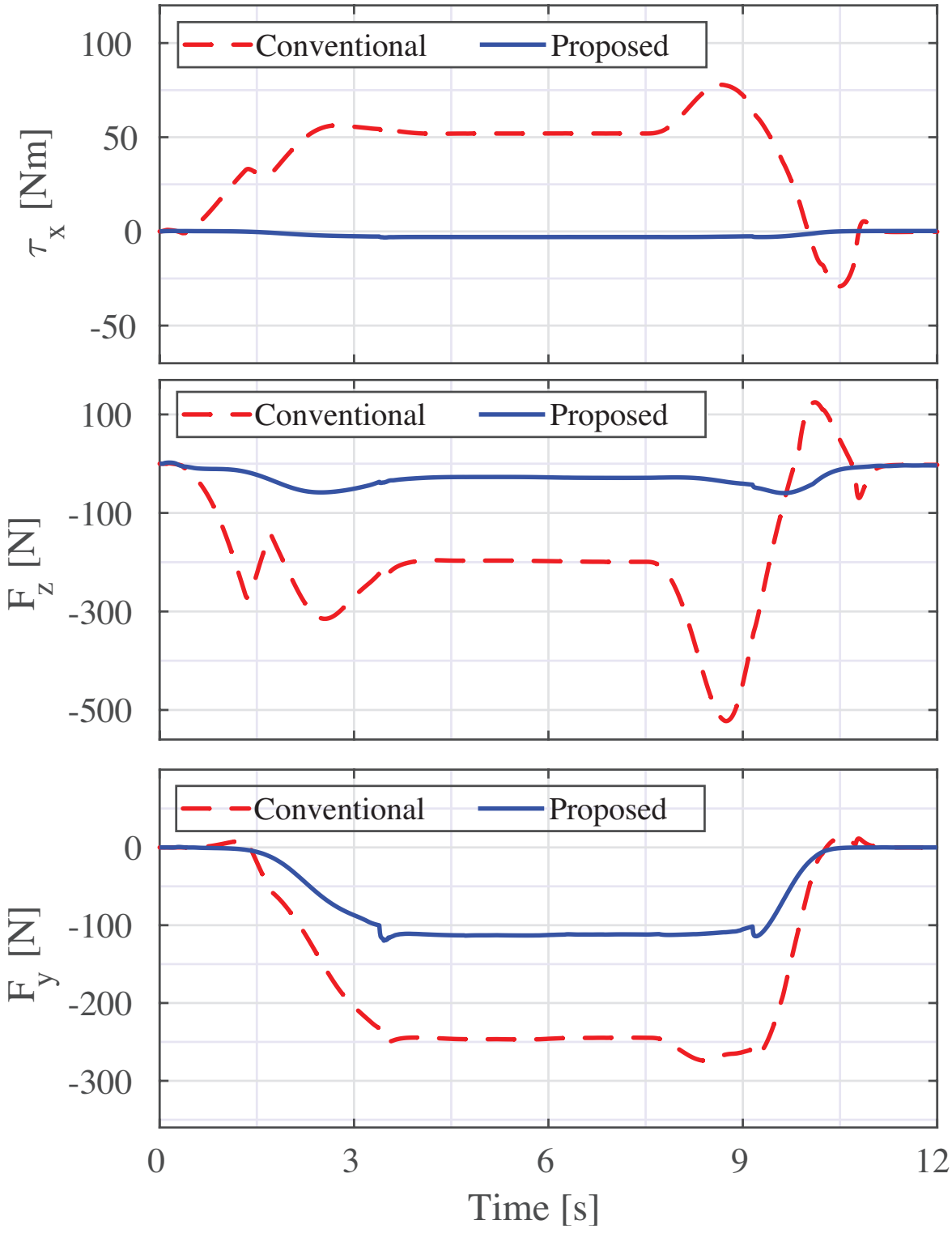


Fig. 6: Interaction force and moments between the human limb and the proposed (solid line) and the conventional (dashed line) braces.

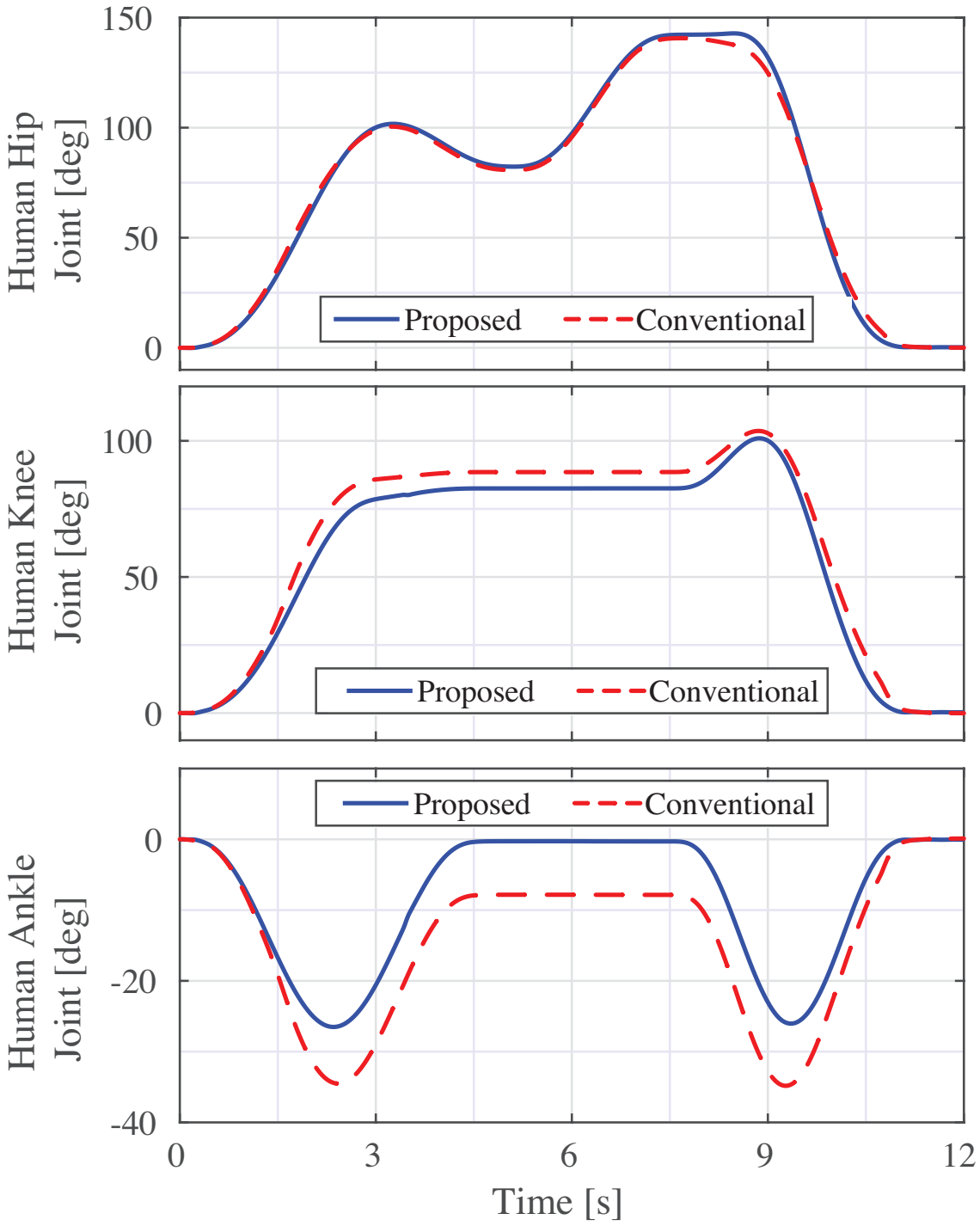


Fig. 7: Variations in the human model's hip flexion/extension, knee flexion/extension, and ankle dorsi/plantar flexion joints for the proposed (solid line) and the conventional (dashed line) braces. The maximum differences between the trajectories are $3.23°$, $6.33°$, and $7.65°$, respectively.

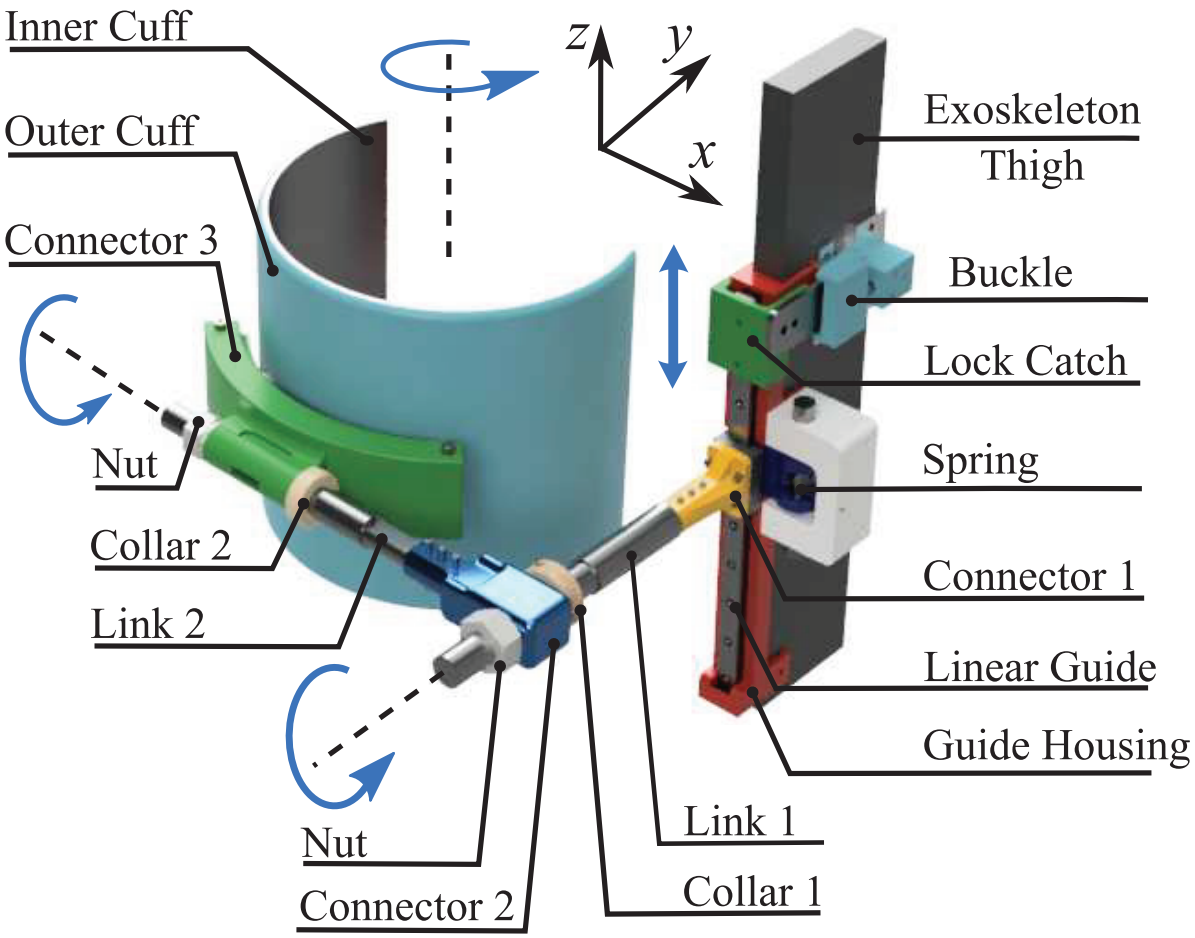


Fig. 8: CAD model of the proposed brace for the right thigh

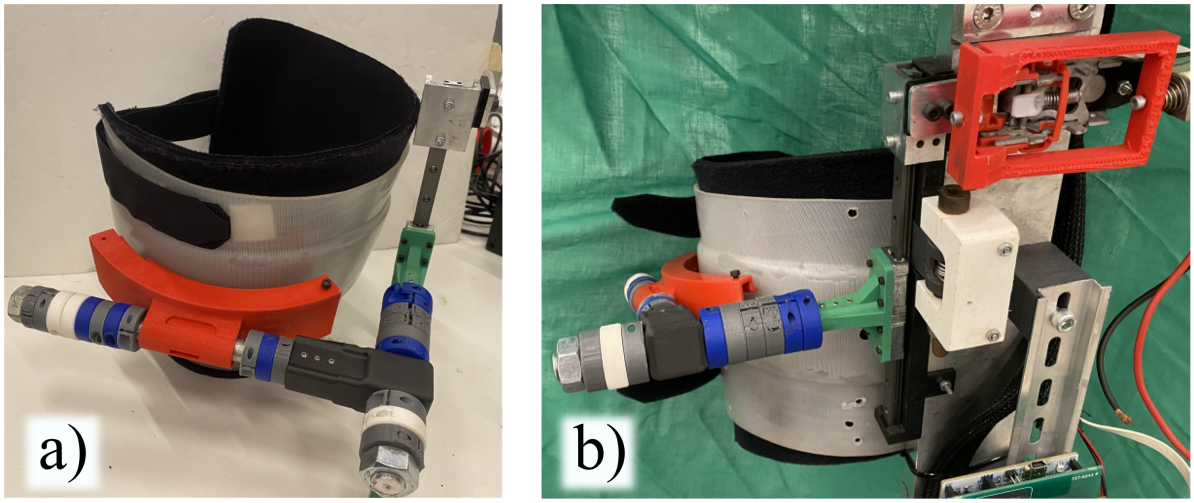


Fig. 9: a) Unmounted brace from the exoskeleton. b) Mounted brace on the exoskeleton.

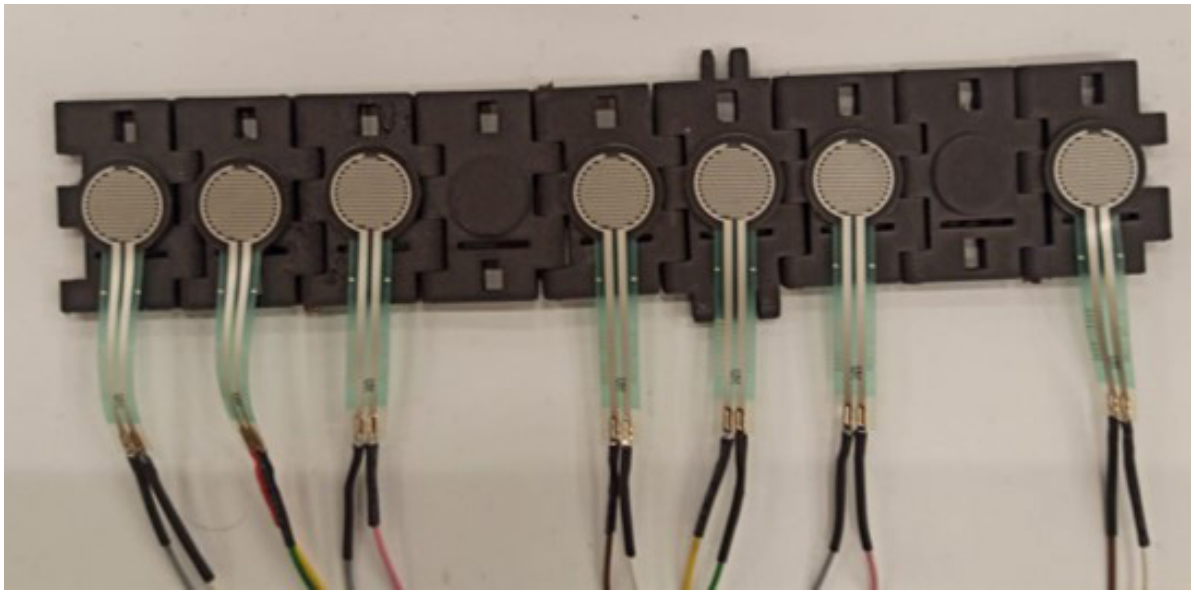


Fig. 10: FSRs are deployed onto the watch strap-like mechanism. The placement of FSRs is for illustrative purposes only and does not reflect any specific measurement strategy.

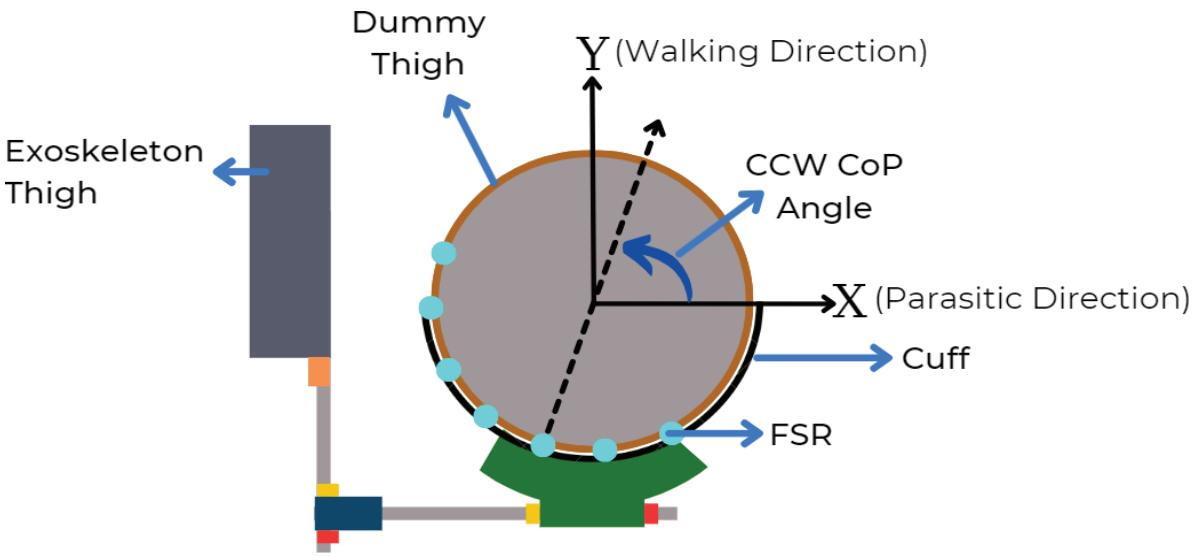


Fig. 11: Top view of the dummy left thigh as tied to the proposed brace.

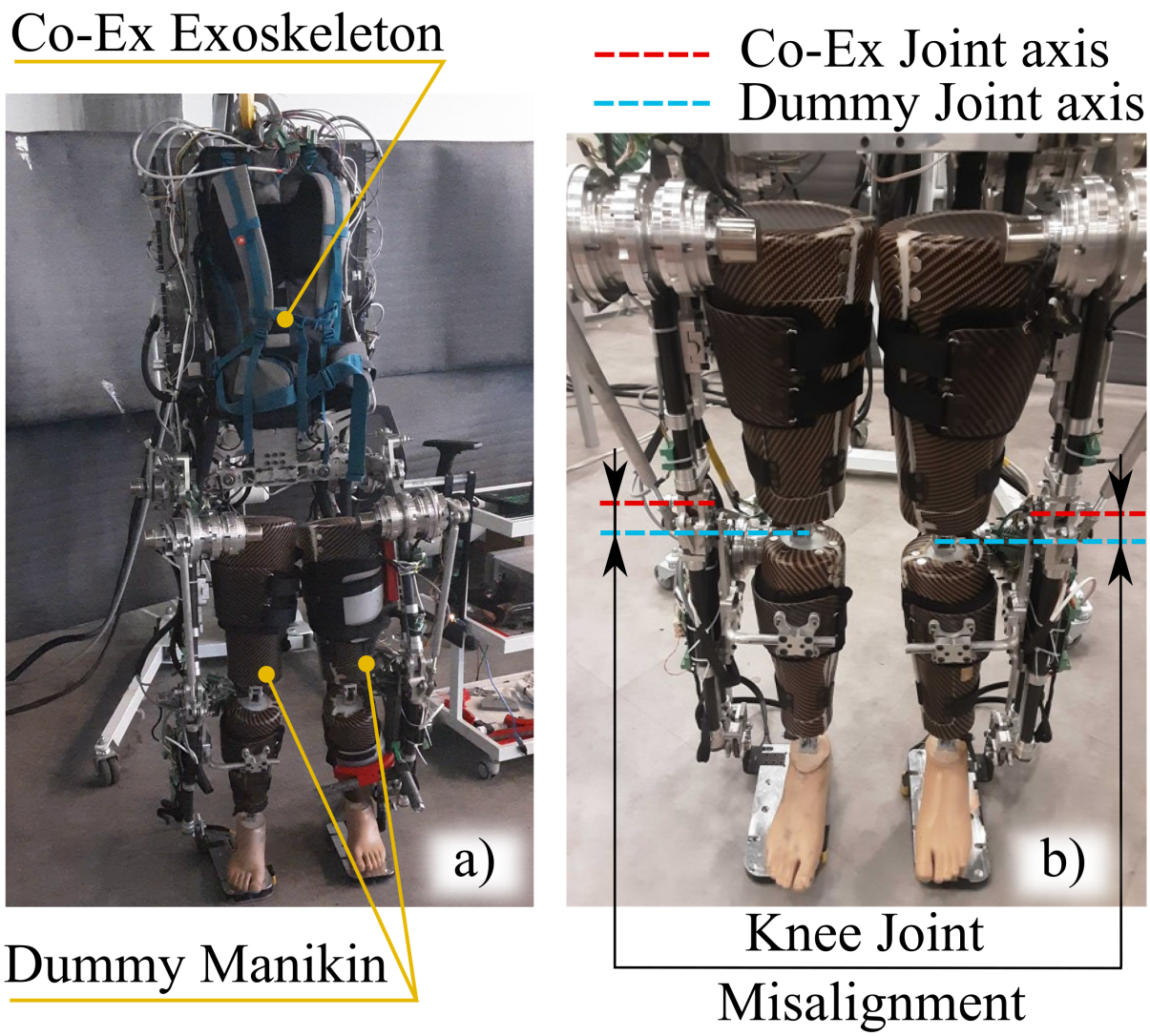


Fig. 12: Dummy manikin tied to Co-Ex: a) Isometric view. b) Front view.

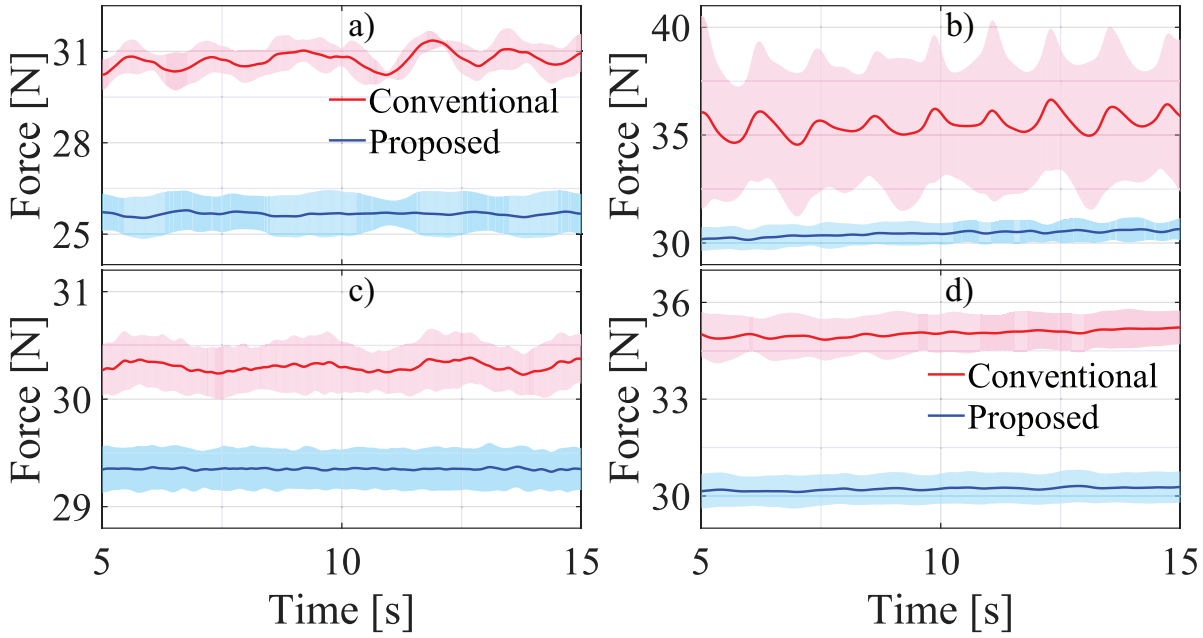


Fig. 13: Force variation observed for the conventional and proposed braces during squatting and swaying experiments.

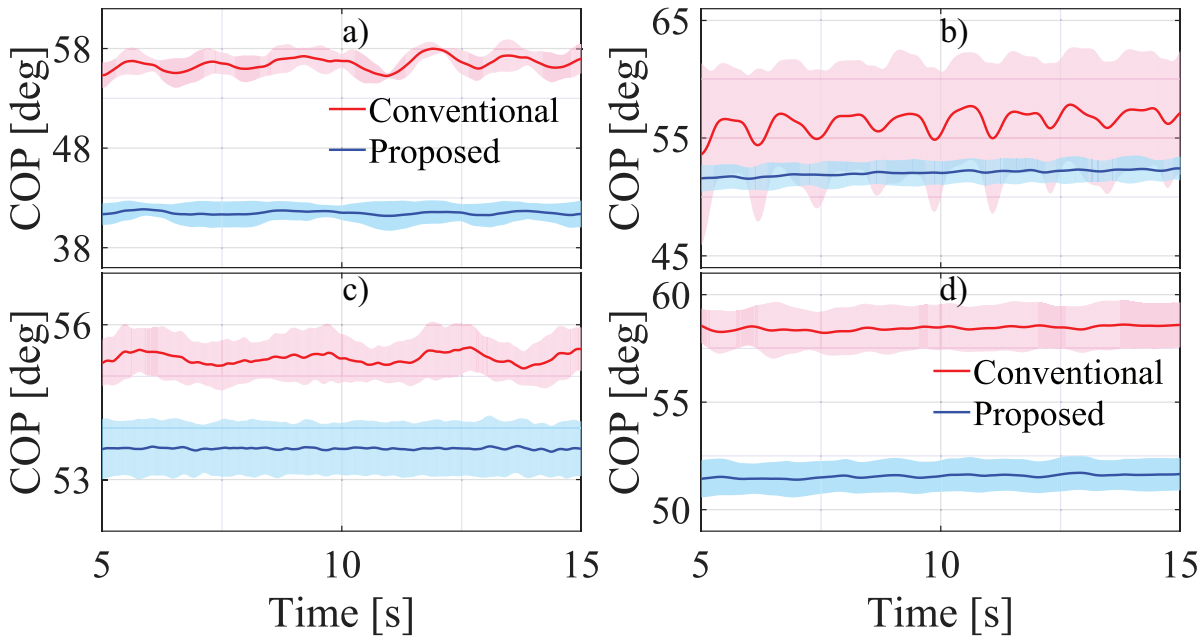


Fig. 14: Center of Pressure (COP) variation for the traditional and the proposed brace during squatting and swaying experiments.

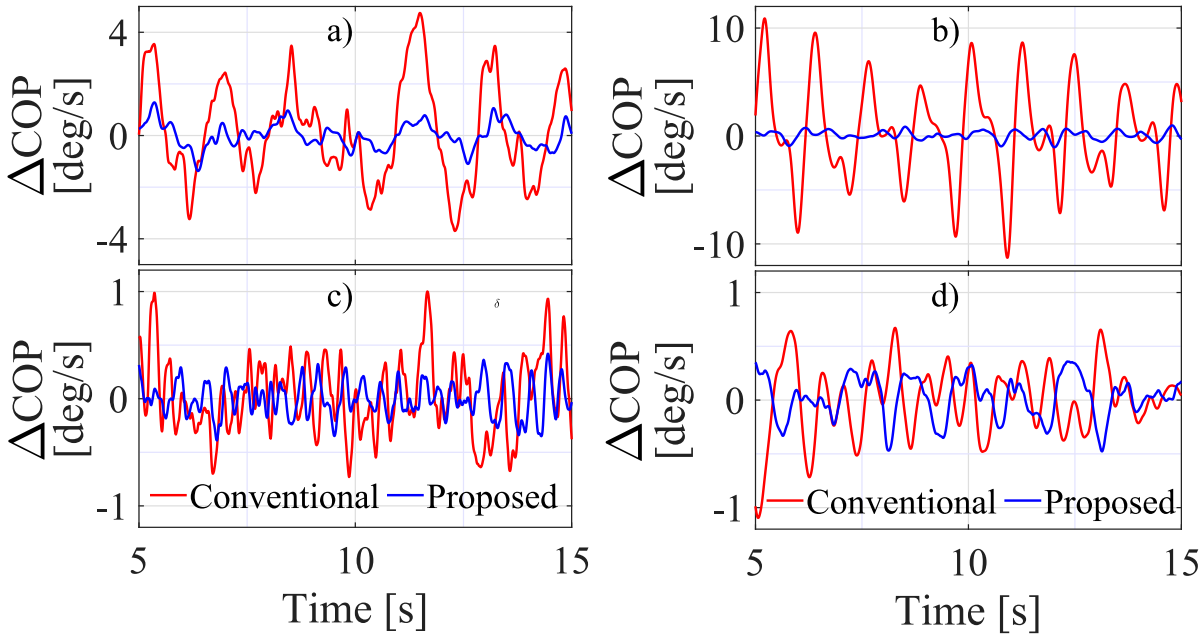


Fig. 15: Rate of change of COP (ΔCOP) variation for the traditional and the proposed brace during squatting and swaying experiments.

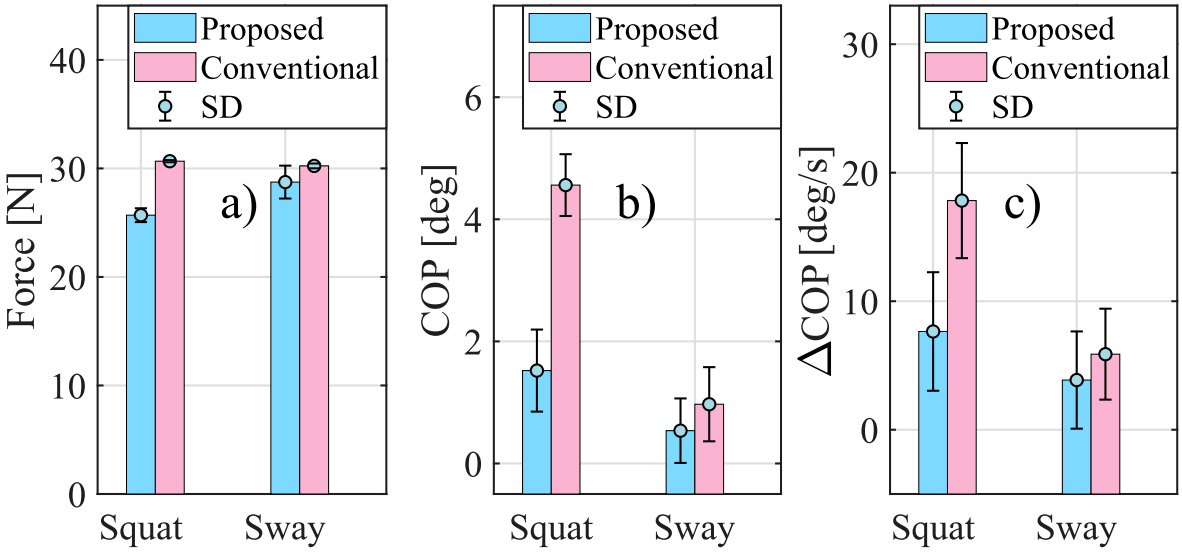


Fig. 16: Mean±SD for each group of eight experiments involving the heavy dummy: (a) average brace force, (b) peak-to-peak COP, and (c) peak-to-peak ΔCOP values.

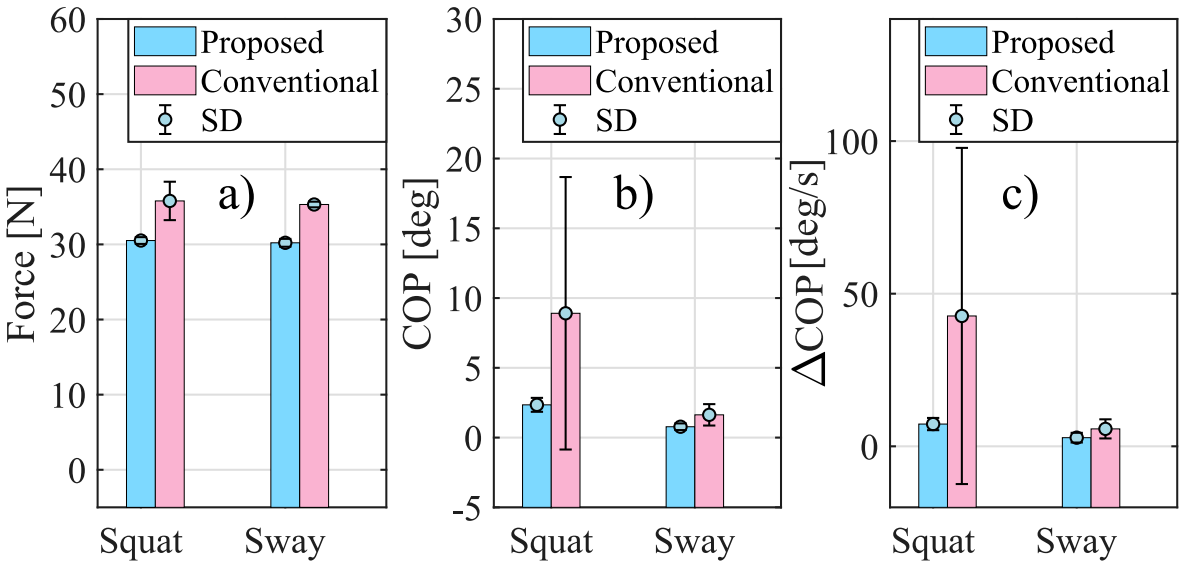


Fig. 17: Mean±SD for each group of eight experiments involving the light dummy: (a) average brace force, (b) peak-to-peak COP, and (c) peak-to-peak ΔCOP values.